Molecular origin of slippery behavior in tethered liquid layers

Fabio Rasera,[†,§] Isaac J. Gresham,[‡,§] Antonio Tinti,[†] Chiara Neto,[*,‡] and Alberto Giacomello[*,†]

[†]*Dipartimento di Ingegneria Meccanica e Aerospaziale, Sapienza Università di Roma, 00184, Rome, Italy*

[‡]*School of Chemistry, The University of Sydney, NSW 2006, Australia*

[¶]*The University of Sydney Nano Institute, The University of Sydney, NSW 2006 Australia*

[§]*These authors contributed equally*

E-mail: chiara.neto@sydney.edu.au; alberto.giacomello@uniroma1.it

Abstract

Slippery covalently attached liquid surfaces (SCALS) are a family of nanothin polymer layers with remarkably low static droplet friction, characterized by a low contact angle hysteresis (CAH$<5^\circ$), which makes them ideally suited to self-cleaning, water harvesting, and anti-fouling applications. Recently, a Goldilocks zone of lowest CAH has been identified for polydimethylsiloxane (PDMS) SCALS of intermediate thickness (≈ 4 nm), yet, molecular-level insights are missing to reveal the underlying physical mechanism of this elusive, slippery optimum. In this work, the agreement between coarse-grained molecular dynamics simulations and atomic force microscopy data shows that nanoscale defects, as well as deformation for thicker layers, are key to explaining the existence of this 'just right' regime. At low thickness values, insufficient substrate coverage gives rise to chemical patchiness; at large thickness values, two features appear: 1) a waviness due to a previously overlooked lateral microphase separation occurring in polydisperse brushes, and 2) layer deformation due to the contact line is larger than in thinner layers. The most pronounced slippery behavior occurs for smooth PDMS layers that do not exhibit nanoscale waviness. The converging insights from simulations, experiments, and a CAH theory provide design guidelines for tethered polymer layers with ultra-low CAH.

Keywords

polymer brushes, PDMS, contact angle hysteresis, MD simulations, AFM mapping

Slippery Covalently Attached Liquid Surfaces (SCALS) are an emerging class of materials consisting of chemically attached liquid polymer chains (i.e. glass transition temperature T_{g} below ambient).[1,2] SCALS exhibit exceptional properties, such as easy droplet shedding, self-cleaning, ice-shedding, and anti-biofouling, often equivalent to lubricant-infused[3] and superhydrophobic surfaces.[4] SCALS are regarded as more robust than other super-wettability surfaces,[5] as their performance does not rely on a specific surface texture or an easily depleted infused liquid lubricant.[2] To date, the most promising SCALS are made of polydimethylsiloxane (PDMS), which is non-toxic, FDA approved, and harmlessly degrades in environmental conditions, and therefore is applicable in a wide range of contexts, from medical devices to atmospheric water capture. SCALS are timely eco-friendly coatings that could replace some perfluorinated ‘forever chemicals’ in anti-fouling.[6–9]

The exceptional performance of SCALS is quantified by measuring contact angle hysteresis (CAH, the difference between advancing and receding contact angle in the limit of zero contact-line velocity), which is proportional to droplet static friction[10] and correlates well with desirable properties such as anti-fouling and anti-scaling.[1] The extremely low CAH ($\approx 1^\circ$), and the corresponding high performance possible with SCALS, superior to alkyl self-assembled monolayers,[11] is attributed to their nebulous ‘liquid-like’ nature. The mechanism by which a liquid-like layer exhibits low CAH is unclear; the low CAH of SCALS has been attributed to the molecular mobility of the tethered chains.[2,12–14] However, as CAH in the limit of zero contact line velocity is a pseudo-static phenomenon, an explanation based on static phenomena would be appropriate.

SCALS belong to the broader family of end-tethered polymer layers, which, at high grafting density, form polymer brushes. The defining feature of SCALS is that the tethered polymers are in a liquid state and hence do not require solvation to be effective. This is in contrast to traditional polymer brushes; for example, polyethylene oxide brushes are only expected to be antifouling when hydrated. As shown schematically in Fig. 1a, the structure and behaviour of tethered polymers is often explained by a single parameter: the reduced grafting density, Σ, which is a measure of the degree of chain crowding:[15]

$$\Sigma = \sigma \pi R_\mathrm{g}^2 \tag{1}$$

where R_g is the average radius of gyration of the grafted polymers (dependent on chain length and solvent quality) and σ is the grafting density (grafting points per unit area, gps/nm^2). $\Sigma < 1$ corresponds to a sparse pancake/mushroom regime where chains form globules that do not interact with each other, while $\Sigma \gg 1$ corresponds to the brush regime, wherein steric crowding forces chains to extend away from the substrate. A transitional 'mushroom-to-brush' regime for $1 < \Sigma < 5$ is typically identified in conventional solvated brush systems. It should be emphasized that Σ is a function of the polymer solvation state, so layers may transition from mushroom to brush states *via* a change in solvent quality. Given that the present work focuses on the PDMS-water system, all Σ values here assume an unsolvated polymer; that is, R_g is that of a sphere with the same volume as the polymer chain.

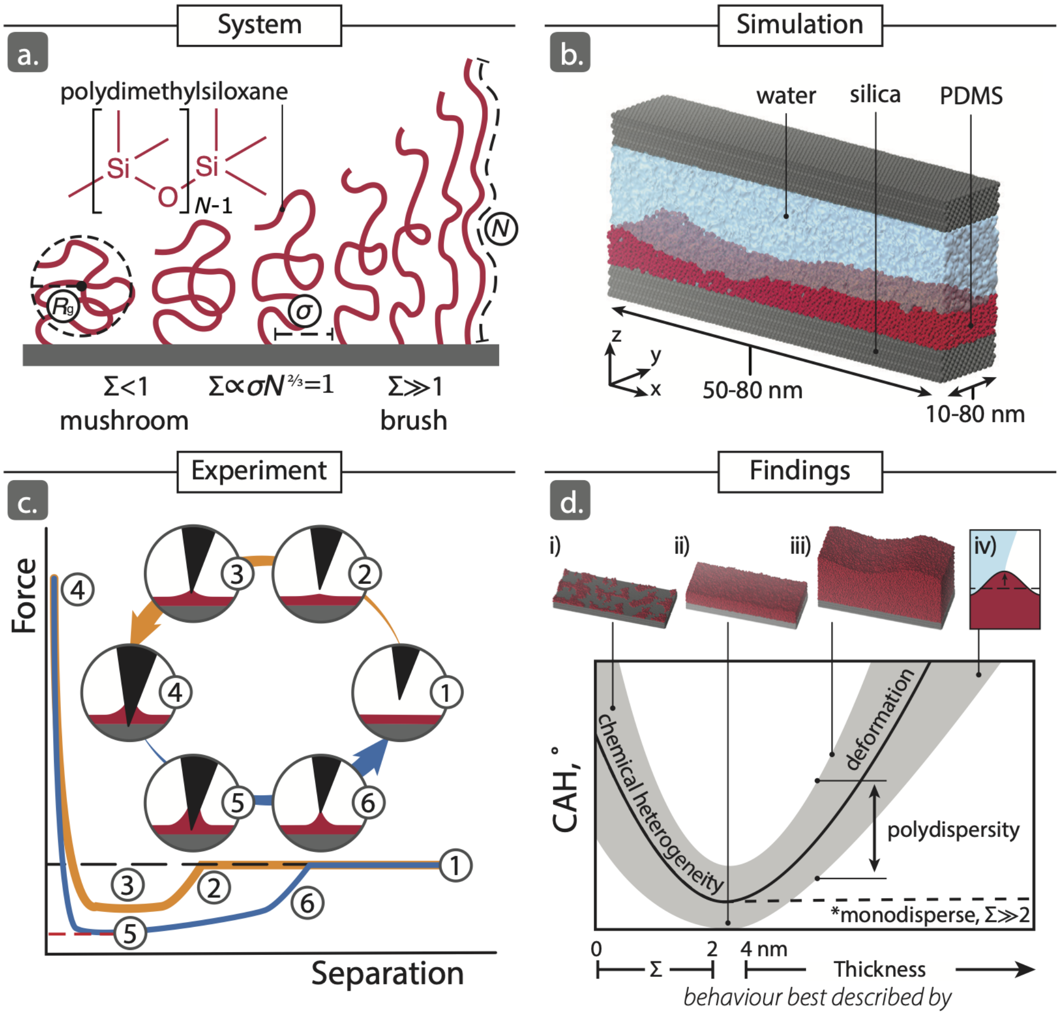

Figure 1: **Combined simulation and experimental study of CALS** a) CALS consist of end-tethered PDMS chains, which can be defined by their grafting density σ and average chain length $\widehat{N}$. Reduced grafting density, Σ, is a powerful predictor of slippery performance. b) Example of a simulated system, which predicts that long chain, polydisperse CALS form wavy structures. c) Meniscus force mapping can distinguish the liquid layer from the underlying solid surface. d) Schematic illustrating the literature trend and the mechanisms identified in this study: i) CAH of thin layers is dominated by chemically heterogeneity, best described by Σ; ii) the lowest CAH is obtained for smooth layers without waviness and deformation; iii)-iv) CAH of thick layers is dominated by layer deformation, which tends to scale with thickness. At all thickness values, polydispersity increases CAH by increasing layer waviness (iii). Due to synthetic techniques, Σ and thickness tend to scale proportionally to one another; producing layers that break this trend is of interest. For instance, monodisperse, high density layers are expected to have low CAH at all thickness values (dashed line).

Extensive literature has identified a 'Goldilocks zone' of lowest water CAH at intermediate layer thickness and/or chain length, as schematically shown by the parabolic trend in Fig. 1d.[2,12,16–21] The exact location of this Goldilocks zone is dependent not only on the techniques used to approximate thickness or chain length, but likely also depends on the precise combination of chain length, grafting density, and polydispersity produced by specific synthetic methods. However, across existing literature the optimum thickness for PDMS SCALS is consistently between 3 and 5 nm.[1] The shaded region around the parabola shows that, both within and between studies, apparently similar PDMS layers (in thickness, composition, contact angle) have different CAH values; extremes between 1° (corresponding to slippery surfaces) and 15° (non-slippery, hence referred to as CALS) have been reported.[1,2,19] This Goldilocks zone also appears to exist for droplets of other liquids,[1,14,17] but there is insufficient evidence to conclude that the CAH minimum occurs at the same thickness or Σ as the water system. Indeed, the framework we propose predicts a change in the minimum due to an increase in Σ in good solvent systems. The molecular origins of these drastic performance differences are only beginning to be understood. Recently Gresham *et al.* demonstrated that Σ is a good predictor for the Goldilocks region for SCALS prepared with different methods, with minimum CAH obtained around $\Sigma = 2$.[12] Covariance between relevant parameters such as average chain length ($\widehat{N}$), σ, thickness ($\propto \sigma\widehat{N}$) and Σ ($\propto \sigma^{2/3}\widehat{N}$)[12] make the exact properties responsible for SCALS behavior difficult to determine experimentally. From this summary of the state of the art, two outstanding questions emerge:

1. What causes the widely-observed parabolic trend and corresponding Goldilocks zone?
2. Why do otherwise identical PDMS layers exhibit different CAH?

In this work coarse-grained molecular dynamics (CG-MD) simulations, informed by experimentally measured physicochemical parameters (chain length, polydispersity, grafting density),[12] were used to address these two questions. Key findings from the simulations are shown in Fig. 1d: i) low Σ CALS are chemically heterogeneous, with patches of the substrate exposed, while iii) in thicker layers, polydispersity induces nanoscale lateral waviness. Low CAH surfaces are ii) chemically uniform and smooth. These simulation features were experimentally observed by adapting atomic force microscopy meniscus force mapping (MFM) to these nano-thin PDMS layers (Fig. 1c). Simulations found that thick layers deform at the droplet three-phase contact line (iv). This deformation has recently been identified as a potential cause of hysteresis in such layers,[19] with comparisons made to wetting on macroscopically soft surfaces (i.e., cross-linked PDMS gels).[9] By applying simple wetting models to the simulated structures, mechanistic explanations for the questions posed above are offered.

Results

The key strength of this work is the combination and close agreement between simulations and experiments, with key layer properties shown in Table 1. Using CG-MD, grafted PDMS layers characterized by different chain length (N), chain length distribution (polydispersity, PDI) and grafting density (σ) were simulated in vacuum and in water, which are both poor solvents for PDMS. A CG force field specific for PDMS was used, which allowed modeling of realistic PDMS behavior.[22] PDMS molecules were grafted to a flat, silica-like substrate,[23] and allowed to equilibrate from the fully elongated configuration. Different realizations of chain lengths and grafting points were simulated. The chain length distribution in simulations mimicked that measured in experiments (see Fig. S1). Simulated layers named P1, P2, and P3 in Table 1 correspond to low, intermediate and high values of average polymer repeat units ($\widehat{N}$), respectively, and are polydisperse (PDI = 1.3-1.35). For all $\widehat{N}$, a range of experimentally relevant grafting densities were simulated (Table 1). System P2, of intermediate thickness and chain length, corresponds to the SCALS with the lowest CAH (2.7°) as previously reported,[12] while systems P1 and P3 are not slippery in experiments. Three monodisperse layers, M50, M100, and M300 (PDMS chains with 50, 100, and 300 monomers) were also simulated for comparison, as shown in the Supplementary information and in Fig. S2 and

Fig. S3.

Table 1: Structural parameters of grafted PDMS layers studied in this work in both simulations and experiments: $\widehat{N}$ = average number of repeat units in the polymer chains, PDI = chain polydispersity, σ = grafting density and d =layer thickness. Simulated layers P1 - P3 are informed by experimental parameters and are polydisperse, while layers M50 - M300 are idealised and monodisperse. Sim. small and Sim. big refer to simulation base areas of 50x10 and 80x80 nm^2, respectively.

Sample		$\widehat{N}$	PDI	σ, gps/nm^2	d, nm
P1	Sim. small	15	1.3	0.1/0.2/0.3/0.6/1.0	0.8±1/0.9±0.2/1.0±0.2/1.3±0.2/2.1±0.2
	Sim. big			0.3	0.9±0.2
	Exp.[†]	8/NA	1.4/NA	0.9/NA	0.9/1.1
P2	Sim. small	88	1.3	0.1/0.2/0.3/0.6/1.0	1.9±0.4/2.6±0.4/3.7±0.5/6.8±0.2/11.7±0.3
	Sim. big			0.3	3.5±0.5
	Exp. (3 nm) [†]	32/88	1.1/1.3	0.75/0.26	3.1/2.9
	Exp. (5 nm) [†]	91/-	1.1/-	0.51/-	5.94/-
P3	Sim. small	308	1.35	0.1/0.2/0.3	4±1/8±1/12±2
	Sim. big			0.3	12.0±0.8
	Exp.[†]	142/308	2.3/1.4	0.44/0.21	8.1/8.1
M50	Sim. small	50	1	0.1/0.2/0.3/0.6/1.0	1.4±0.5/1.8±0.5/2.2±0.7/4.0±0.5/6.5±0.3
M100	Sim. small	100	1	0.1/0.2/0.3/0.6/1.0	2.0±0.8/3±1/4.0±0.2/7.8±0.3/12.9±0.4
M300	Sim. small	300	1	0.1/0.2/0.3	4.0±0.5/7.9±0.3/11.6±0.3

[†] For experimental systems, two values are reported, respectively: measured by (reflectometry + numerical self-consistent field theory)/(measured by ellipsometry + single-molecule force spectroscopy). Experimental values shown here are obtained from.[12]

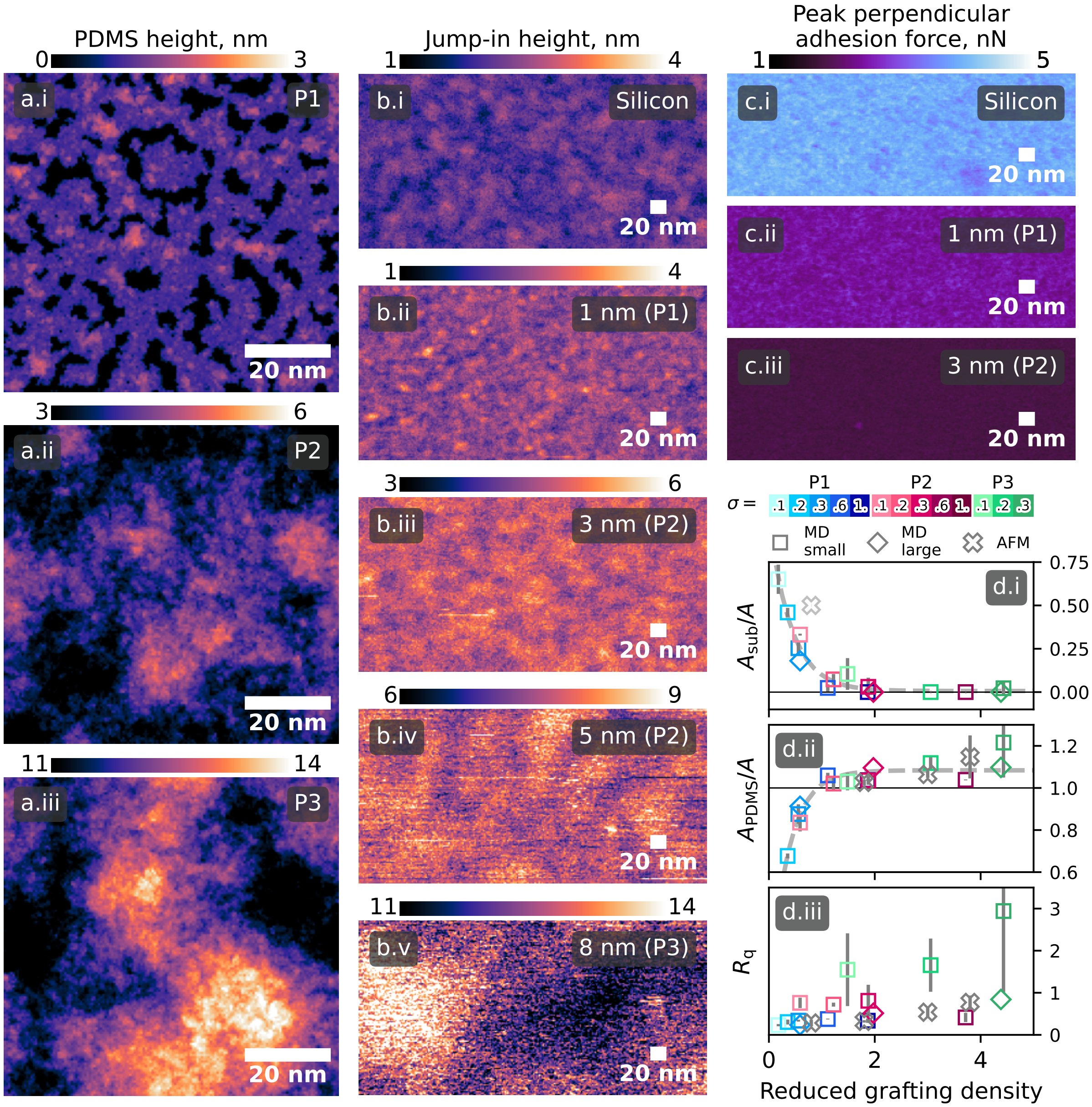

Figure 2: **Surface topography of PDMS CALS**: (a) predicted by MD and (b) measured by MFM, for increasing Σ (Table 1). (b.i) MFM image of unmodified silicon wafer (non-zero jump-in due to humidity). (c) Peak adhesion maps from MFM. P1, the low Σ PDMS layer, has a chemically heterogeneous surface, with peak adhesion values between that of silica (c.i) and that of thicker PDMS layers (c.iii). (d) Parameters derived from panels a-c, plotted as a function of Σ: (d.i) area of silica accessible to the contacting liquid divided by the projected surface area, (d.ii) area of PDMS accessible to the contacting liquid divided by the projected surface area, and (d.iii) RMS roughness of the PDMS layers. Colour corresponds to N and σ; markers denote values derived from 50×10 nm^2 MD boxes (□), 80×80 nm^2 MD boxes (◇), and AFM images (×).

The experimental PDMS layers were prepared using the synthetic method of Krumpfer and McCarthy.[17] Highly detailed data on layer structure was obtained from previous work by Gresham *et al.*,[12] as shown in Table 1. CAH was assessed by adding/withdrawing volume from a water droplet quasi-statically and measuring the advancing/receding contact angle. New experimental data consists of AFM maps of topography and adhesion force for the grafted PDMS layers. The Bruker Multimode Peakforce Imaging AFM mode was used to produce force–distance curves at every point of the scanned area. From the force-distance curves, meniscus force measurements (MFM) were taken: the position of the jump-in at which the liquid meniscus touches the AFM tip was extracted using a custom script, and this allowed to reconstruct the nanoscale topography of the liquid layer.[24] A similar approach has been developed by Zhou *et al.*[19] Peakforce imaging was used as it was challenging to accurately track the surface of these liquid layers with conventional tapping-mode AFM, as discussed further in Supplementary Information.

Chemical and topographical nanoscale defects in grafted surfaces

The CALS topography produced by MD simulations and measured by MFM are presented in Fig. 2, and show experiment and simulation in excellent agreement. Broadly, both simulation and experiments featured chemically heterogeneous layers at low Σ (Fig. 2a.i, b.ii), which transitioned into chemically homogeneous layers at intermediate Σ (Fig. 2a.ii, b.iii, b.iv). As Σ increased further, the surfaces remained chemically homogeneous, but an unexpected topographical waviness of low aspect ratio emerged in both simulations and experiments (Fig. 2a.iii, b.v). Simulations show that such waviness is always in full contact with water. The trends observed in the presented images are supported by additional simulations, summarised in Fig. 2d. Figure 2d.i shows that at $\Sigma < 2$ the area of the substrate accessible to the contacting liquid (A_{sub}) is a significant fraction of the entire projected surface area (A), indicative of a chemically heterogeneous surface. At higher Σ values, Fig. 2d.ii demonstrates that the surface area of the PDMS layer (A_{PDMS}) exceeded that of the planar substrate, corresponding to the appearance of waviness. The formation and growth of these wave-like features is also captured by the increase in RMS roughness (R_q) with Σ observed in Fig. 2d.iii. The RMS roughness agrees well with the values measured previously by Cheng *et al.*,[14] which vary between 0.33 and 0.75 nm, with a minimum value obtained at intermediate chain length. Results derived from simulations (colored markers) match those measured experimentally (grey crosses), both in absolute terms and in the trends observed.

A detailed comparison of simulated and experimental results in Fig. 2 is provided here, starting at low Σ and proceeding to higher values. The simulated low chain length surface (P1) was patchy at σ values below 0.6 gps/nm^2, with large fractions of the bare substrate (between 70 and 15%, shown in black in Fig. 2a.i) exposed to the contacting liquid (blue data points in Fig. 2d). As expected, the exposed substrate area decreased with increasing grafting density, with full coverage only reached at the highest $\sigma = 1$ gps/nm^2. Overall, the P1 surface showed strong chemical heterogeneity in simulations, but the patches of bare silica could not be resolved by AFM due to their small size. However, adhesion of the AFM tip to the surface could be used as a proxy of exposed substrate; Fig. 2c shows that the thin PDMS layer in P1 (c.ii) had intermediate adhesion (≈ 3.2 nN) between that of an uncoated silica native oxide layer (c.i, ≈ 4.5 nN) and that of a thicker PDMS layer (c.iii, ≈ 2 nN). From these measurements, a coverage of 50% is approximated and plotted in Fig. 2d.i as a grey cross. Maps of the peak adhesion value for P1 (Fig. 2c.ii) were more heterogeneous than those for thicker PDMS layers (Fig. 2c.iii), supporting the presence of the chemical defects seen in the computation.

The simulated intermediate chain length surface (P2) showed lower chemical heterogeneity than P1, with a significant fraction of exposed substrate observed only at the lowest grafting density, $\sigma = 0.1$ nm^{-2} (Fig. 2d.i). Surprisingly, the layer topography was not entirely smooth even for full substrate coverage, as might have been expected for a liquid interface. Instead, the emergence of waviness was observed, with an amplitude on the scale of 1 nm and a wavelength of approximately 20 nm (Fig. 2a.ii). These features became more pronounced as layer thickness increased further. For the high chain length surface (P3) in Fig. 2a.iii, the waviness had an amplitude of ≈ 5 nm and wavelength around 50 nm, and was observed at all grafting density values studied, leading to an increase of A_{PDMS}/A above 1 and to a growing R_q (Fig. 2d.ii and d.iii). AFM maps of comparable surfaces confirmed this surface topography (Fig. 2b.iii), although, for layers with comparable thicknesses and/or Σ, the wavy features observed experimentally had larger wavelength and slightly lower amplitude than in simulations. Still, the overall trend remained remarkably close, with waviness size increasing as Σ increased.

The waviness observed here is a static feature, both in simulations and experiments, and as such cannot be rationalised as capillary waves, as have been observed at liquid-air interfaces. Further investigation of the origin of these features (discussed below) confirm they are expected to be static. Furthermore, the MFM technique enables the simultaneous determination of the substrate and layer topography, which allowed us to exclude that substrate topography is at the origin of the wave-like features observed. Furthermore, maps of the maximum adhesion force became uniform as Σ increased (Fig. 2c.iii), indicating that the higher Σ layers were chemically homogeneous.

The waviness predicted by MD simulations and revealed by MFM is the most unexpected element of Fig. 2. Because the polymers are above their T_{g} ($T_{\mathrm{g}} < -100$°C for PDMS) and grafted relatively sparsely, it has been argued that the layer would self-smooth on all length scales,[25] as would be observed for a true liquid interface. However, these tethered-liquid polymer layers are shown to be heterogeneous both in terms of their chemistry (at $\Sigma < 2$) and of their topography ($\Sigma > 2$). From this observation two questions arise: what is the origin of these features, and can they explain the Goldilocks minimum in CAH observed across the literature? Both questions are discussed in turn in the following sections.

Polydispersity induces waviness

The nanoscale waviness observed for polydisperse cases is reminiscent of the phenomenology of microphase separation, common in block copolymers and mixed polymer brushes.[26–28] However, to the best of our knowledge, this microphase separation has not been previously reported for liquid-like grafted polymers of a single monomer type. Below, these features are shown to be due to polymer segregation based on chain length, which occurs both vertically and laterally. While these segregation modes are inexorably linked, vertical separation will be discussed first, as it has previously been predicted by theoretical approaches, before turning to the more novel lateral separation of homopolymers.

Vertical phase separation can be clearly seen in the histograms adorning the side of Fig. 3a

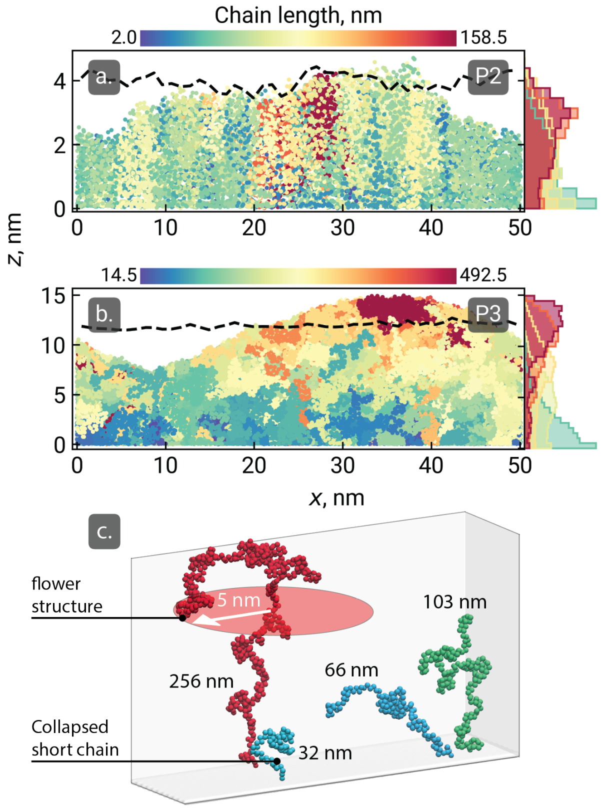

Figure 3: **Waviness is caused by length-wise segregation of chains:** a,b) cross-sectional profiles of P2 and P3 layers ($\sigma = 0.3$ nm^{-2}), with chains colored according to contour length. Different chain length fractions segregate to form wavy features; vertical chain segregation is captured by the accompanying histogram, which compares favorably to theoretical results (Fig. S4).[29] Comparable monodisperse layers (M100 and M300, respectively) do not develop waves; their surfaces are plotted as dashed lines. c) Conformations of different length chains in b, showing the flower structure of long chains (red). The R_g of chains in the flower regime (red circle) is not large enough to cover the whole surface, hence the emergence of waviness.

and b, which shows the segregation of chains based on their contour length. Short chains coil close to the substrate (even though their contour length is sufficient for them to extend throughout the layer; compare colorbar and y-axes scale), intermediate chains are relatively stretched and dispersed throughout the layer, and longer chains stretch to the top of the layer (Fig. 3c), where their apical segments coil in flower-like aggregates. This partitioning of longer chains to the brush-solvent interface (named flower-stem) is predicted by numerical self-consistent field theory (nSCFT),[29–31] a mean-field technique that successfully described polymer brush behaviour in a number of contexts.[12,32–34] de Vos and Leermakers[29] model the structure of a polydisperse brush with nSCFT and plot the volume fractions of polymers with different lengths, which nicely match the histograms in Fig. 3a and b (see Fig. S4); fundamental work on bi-disperse brushes also report similar phenomena.[35–37] The excellent agreement between the vertical phase separation predicted by our simulation and nSCFT support our subsequent observation of lateral separation.

Figure 3b shows that the vertical and lateral segregation are linked: longer chains concentrate at the bulge of the waves, medium chains at the troughs, and shorter chains at the bottom of the layer. This behaviour can be rationalised by considering a bidisperse brush, in which the longer polymers extend past the shorter polymers (the stem) and spread into a flat (the crown) aggregate. In the same way, in polydisperse systems, chains sufficiently longer than the average coil over the rest of the layer as the effective chain crowding decreases far from the substrate. The characteristic size of the bumps is determined by the gyration radius of the 'flower' segments of the longer chains $R_{g,f}$ above the average brush thickness[36] (Fig. 3c). If the number of flower structures is not sufficient to entirely cover the surface, i.e., if the reduced grafting density of flowers $N_f \times R_{g,f}^2/A < 1$, then surface waviness must emerge.

Given the mechanism behind waviness, both the amplitude and the wavelength of the features in Fig. 2 are expected to depend on $R_{g,f}$ and thus to increase with increasing mean chain length. For instance, in P3, chains have lengths ranging up to ca. 500 nm with an average of 300 nm, while for P2 the maximum is only 125 nm, with an average of 90 nm. Additionally, going from P1 to P3 a progressive stretching of the PDMS layer is observed in the middle of the layer, while the top of the layer is coiled (Fig. 3c). Monodisperse CALS do not develop the waviness predicted for their polydisperse counterparts (smooth surfaces plotted in Fig. 3a, b as dashed lines).

In summary, Fig. 3 shows that the emergence of waviness in sufficiently thick, polydisperse PDMS layers is related to the way in which chains of different length self-organise in the layer.

Making sense of contact angle hysteresis

It is well established that both chemical defects (as in P1, Fig. 2) and topographical roughness (the waviness most pronounced in P3, Fig. 2) result in CAH.[38,39] As the P2 sample, which corresponds to the lowest CAH experimental sample, appears to have no chemical defects (compared to P1) and less waviness (compared to P3), it is tempting to use these features to answer the two questions posed in the introduction. To do so quantitatively, a simple theory linking chemical defects and waviness to CAH is presented below.

The classical model for static CAH by Joanny and de Gennes[38] and its extensions relate CAH to the number of defects and to the energy dissipated by a defect in an advancing/receding cycle.[38,40,41] The nanoscale defects present in CALS can collectively give rise to hysteresis, because each of them may exert a small pulling (upon receding) or pushing force (upon advancing) on the liquid front. Following the model of Ref.[42] for nanoscale defects (both chemical and topographical) in the dilute regime, the energy dissipated by defects during an hysteresis cycle is estimated from their wetting free-energy weighted by the area fraction they occupy, see Supplementary Information for details:

$$\begin{aligned}\mathrm{CAH} &\equiv (\cos\theta_r - \cos\theta_a) \approx (\theta_a - \theta_r)\sin\theta_e \\ &= \frac{1}{2}\frac{A_{\mathrm{sub}}}{A}|(\cos\theta_{\mathrm{PDMS}} - \cos\theta_{\mathrm{sub}})| + \frac{1}{2}\frac{A_{\mathrm{PDMS}} - (A - A_{\mathrm{sub}})}{A}|\cos\theta_{\mathrm{PDMS}}| \qquad (2)\end{aligned}$$

where θ_r and θ_a are the receding and advancing contact angles, the equilibrium contact angle is defined as $\theta_e = (\theta_a + \theta_r)/2$, A_{sub} is the surface area occupied by chemical defects, A_{PDMS} is the total PDMS area accessible to the contacting liquid, and A is the projected area of the substrate. θ_{sub} and θ_{PDMS} are the values of the Young contact angle on the bare substrate (silica) and on a flat PDMS layer, respectively. The factor 1/2 is due to the assumption that the maximum force a defect can exert on the liquid front, and thus the dissipated energy, coincides, on average, with the defect being half covered by the liquid. The approximation in Eq. 2, CAH$\approx (\theta_a - \theta_r)\sin\theta_e$, is valid for small CAH;[10] for hydrophobic equilibrium contact angles, as PDMS for which $\theta_e = 105°$,[23] the expression further reduces to CAH$\approx \theta_a - \theta_r$. Eq. (2) takes into account both the effect of chemical defects, characterised by the wetting contrast $(\cos\theta_{\mathrm{PDMS}} - \cos\theta_{\mathrm{sub}})$ with area fraction A_{sub}/A (introduced in Fig. 2d), and of topographical ones, which result in an excess area $A_{\mathrm{PDMS}} - (A - A_{\mathrm{sub}})$ compared to the flat silica surface. This excess area is related to A_{PDMS}/A shown in Fig. 2d. Eq. 2 is an approximate model relating defect wetting energy to CAH, distinct from the usual Cassie-like models that are concerned with the equilibrium contact angle.

Figure 4a shows an overview of literature data and serves as a reminder of the two questions posed in the introduction. Figure 4b highlights the important observation that, for any layer, polydispersity increases the CAH by 1-4°. This effect may explain the discrepancy in the results in the literature. Using the current synthetic methods, the chain length and polydispersity of grafted PDMS chains increase together,[12] and while layer thickness is a useful proxy for chain length, most published reports do not quantify polydispersity. Therefore the variability in published reports on CALS could be a consequence of poor control of polydispersity. Secondly, as described below, polydisperse chains are likely to be more deformable than monodisperse ones, further increasing their CAH.

Figure 4c,d shows CAH computed from Eq. 2 for the simulated systems (modelled CAH), alongside experimental values, plotted against layer thickness d and reduced grafting density Σ. The model predicts the steep decline in CAH at low Σ (and thickness) seen in experiments, with near quantitative agreement when θ_{sub} is set to 31°. For both experiments and simulations, the CAH minimum ($\approx 1.5°$) occurs in the same range of parameter values ($d = 3 - 6$ nm or $\Sigma = 1.5 - 3$). In both c) and d), the minimum in CAH corresponds to the P2 surface that was shown to have the lowest incidence of chemical defects and waviness. However, experimental and modelled values deviate at higher Σ values, with the model in

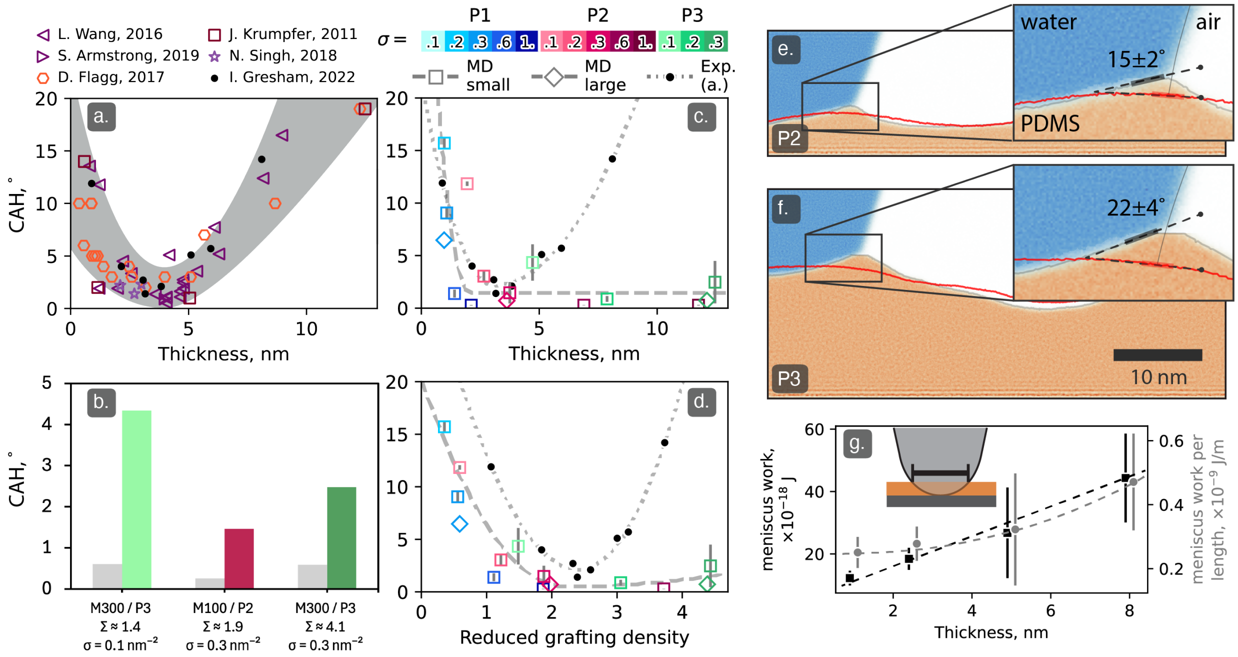

Figure 4: **Emergence of CAH:** a) Contact angle hysteresis as a function of thickness for select literature reports,[1] showing the general trend of CAH vs thickness in CALS. b) CAH for a range of polydisperse and monodisperse surfaces as calculated from simulations *via* Eq. 2; polydispersity increases the CAH by 1-4 °, and as such could explain variation observed in literature for layers of a similar thickness. CAH as a function of c) layer thickness and d) reduced grafting density, as obtained from experiments,[12] (●) and MD simulations (□, ◇) through the use of Eq. 2. Chemical defects explain the general CAH trend for low-Σ layers, but the waviness is not sufficient to explain the CAH of high-Σ layers. Instead, deformation of the PDMS layer around a droplet is likely responsible for the steep increase in CAH at high Σ. e) Simulations of the three-phase contact line show that the (slippery) P2 layer deforms less than the (f) thick P3 layer around a droplet. The local slope of the surface changes by (approximately) 15° and 22° for P2 and P3, respectively, accounting for increased CAH in P3.[43] g) Work done on a retracting AFM tip (here termed the meniscus work, left axis) and normalised meniscus work (divided by the circumference of the tip in contact with the layer, right axis) as a function of the PDMS layer thickness, due to deformation of the liquid meniscus upon retraction of the AFM tip.

Eq. 2 predicting a rather small increase in CAH due to waviness.

One possible source of this discrepancy is that Eq. 2 assumes rigid topographical defects, whereas the wavy PDMS layer is deformable. Deformable surfaces are known to increase CAH as compared to their rigid counterparts because the ‘ridge’ pulled up by capillary forces around the droplet acts as an additional defect.[19,43–45] While the effect of ridge formation on the *dynamic* CAH has been investigated,[21,25] the mechanism is not as well established for static contact line friction. The shear modulus of brushes should increase as $\mu \propto 1/N$,[46,47] so it is expected that $\mu(P3) < \mu(P2) < \mu(P1)$. Our simulations with an explicit three-phase contact line around a droplet show that the ridge pulled up is larger for P3 than for P2 (Fig. 4e,f), consistent with prior work on a thin monodisperse brush.[48] Further simulations of the equilibrated three-phase contact line were conducted for monodisperse layers, revealing that the ridges on monodisperse surfaces exhibit greater symmetry and reduced angularity (Fig. S5). This indicates that a contact line likely experiences less effective pinning in monodisperse layers and, consequently, reduced CAH. Experimentally, the work done by the PDMS meniscus on a retracting AFM tip (hence called meniscus work, measured by integrating the force vs. separation profile,[19]) was used as a proxy for the energy required to deform the layer at the three-phase contact line. The average meniscus work measured in our AFM experiments increases with layer thickness, even when correcting for the effect of contact-line length (Fig. 4g). If the effect of layer deformation on CAH was exclusively geometric, as postulated in Ref.[43] following Gibbs pinning criterion,[49] the additional CAH due to deformation would be significantly higher for P3 than for P2, as the edge angle is 25° and 13°, respectively (Fig. 4e,f). Therefore, a significant increase in CAH is expected as the thickness and thus the deformation of the PDMS layer increases: this feature could thus account for the increased CAH seen in experiments beyond the Goldilocks zone and will be investigated quantitatively in an upcoming work.

Overall, multiple phenomena explain the Goldilocks zone defining SCALS, as summarized in Fig. 1d. Chemical defects cause the high CAH generally seen at low thicknesses; Σ is the appropriate parameter to distinguish the chemically heterogeneous patchy regime from the brush one,[12] i.e., the emergence of chemical defects. On the other hand, layer deformation accounts for the increase in CAH observed at higher thickness; this mechanism has very recently been suggested by others.[9,19] For a given Σ, the deformation (and hence CAH) of the layer should correlate with N.[46] Finally, polydispersity was seen to increase the predicted CAH *via* an increase in layer roughness across CALS of all thicknesses. Hence, polydispersity could reasonably account for the range of CAH reported in literature for ostensibly similar layers. Moreover, the flower-like coils induced by polydispersity consist only of long chains, and hence will be more deformable than the rest of the layer. MD also predicts that layers in the limit of high Σ and low polydispersity should also exhibit low hysteresis, regardless of thickness. These layers are most similar to conventional (tightly packed) self-assembled monolayers. To date, they have not been prepared experimentally.

The explanation of static CAH in terms of the nanoscale features of the grafted surface accounts for some of the important static properties of SCALS, including their water repellency and low droplet adhesion. However, dynamical properties of SCALS, including lubrication and fouling reduction,[1] are not discussed here. Such properties may be related to the mobility of the layer,[12] which cannot be probed directly in this static model. For example, the diffusion of a probe particle could be significantly affected by chemically or topographically heterogeneous surfaces, as reported by fluorescence correlation spectroscopy measurements.[12,19] The anomalous diffusion, however, could be another indirect effect of layer homogeneity rather being the cause of the optimal range of Σ.

Conclusions

In this work, a multiscale approach combining simulations, experiments, and wetting models was used to connect the molecular composition of grafted PDMS layers to their nanoscale surface topography and to their macroscopic properties, in particular, to contact angle hysteresis. The mechanism underpinning the Goldilocks zone of SCALS was clarified, i.e., the occurrence of SCALS behaviour in an intermediate range of layer thickness ($3 - 6$ nm) and reduced grafting density ($\Sigma \approx 2$). On thinner grafted polymer layers, increased pinning of droplet contact line is due to chemical defects, corresponding to exposed patches of the hydrophilic substrate, as the short chain molecules incompletely cover the substrate. On thicker layers, increased pinning occurs due layer deformation. For all uniform layers, polymer dispersity leads to the emergence of previously overlooked nanoscale surface waviness, which we confirm here by both experiments and simulations. This surface waviness can explain the range of CAH reported in literature for layers of similar thicknesses. These results, summarised in Fig. 1d, provide design principles for SCALS: the layer must uniformly coat the substrate ('just right' Σ), minimise deformation ('just right' layer thickness) and have low polydispersity. Conducting MD simulations informed by experimental parameters leads to sophisticated insights that would be impossible with a single approach in isolation.

Methods

Simulations

Coarse grained simulations were conducted using GROMACS 2023.3[50] and interactions were modeled using the most recent MARTINI force field (MARTINI 3[51]). The PDMS chain model is described in Cambiaso *et al.*[22] The simulated systems consist of a hydrophilic substrate ($\theta_Y \sim 75°$), representing the chemical state of a silica surface with an intermediate number of silanol groups.[23,52] The PDMS chains are bonded at random sites, and only one chain can occupy each site. Initially, the chains are in stretched upright positions, then relaxed by steepest descent energy minimization. For each system, a simulation is carried out in vacuum, using an NVT ensemble, until the PDMS layer reaches a stable average thickness and density profile. For the cases in which the chains are very long, this process can take a simulation time in the order of μs. A synoptic view of the thickness of the simulated PDMS layers is reported in Fig. S2. Substrates of 50×10 nm^2 were simulated at different grafting density and producing three realization for each chain length distribution, while larger 80×80 nm^2 MD boxes allowed only for a single representative simulation for P1, P2, and P3. After equilibration in vacuum, the system is solvated and equilibrated again for at least 50 ns (100 ns for the biggest systems), with a mobile piston added to impose a pressure of 1 atm. The water beads are composed of a mixture of 3 bead sizes, a procedure to avoid artificial ordering of water beads near other surfaces and freezing at room temperature.[53]

The length distributions of the polymers in the simulated layers were modelled on experimental distributions obtained by Atomic Force Microscopy (AFM) in Single Molecule Force Microscopy (SMFM) mode.[12] As customary, the polydispersity of polymers is quantified through the Schulz-Zimm distribution:

$$f(N) = \frac{k^k N^{k-1} e^{-kN}}{\Gamma(k)} \tag{3}$$

where N is the chain length, $\Gamma(k)$ is the gamma function of k, and k is a parameter related to the polydispersity index (PDI) through PDI $= 1 + 1/k$. We sampled the Schulz-Zimm distribution using 3 sets of PDI and average chain length $\widehat{N}$ to simulate samples P1, P2, and P3. The PDI and $\widehat{N}$ are directly obtained from a fit of the Schulz-Zimm[54,55] function to the experimental distribution. The actual length distributions after sampling is reported in Fig. S1. The procedure for calculating surface areas is explained in details in Supplementary information and Fig. S6.

Experiments

PDMS CALS imaged by AFM were prepared using the Krumpfer and McCarthy approach,[17] which has been used by numerous groups to prepare PDMS CALS,[20,21,25,56,57] following the method documented in our recent work.[12] Briefly, a few droplets of pure linear PDMS (silicone oil) of different viscosities (P1: 20 cSt, P2: 50 cSt / 350 cSt, and P3: 10 kcSt) were pipetted onto SEMI prime grade silicon wafers (0.675 mm thick, N-type, resistivity 1-20 Ω, orientation $< 100 >$). PDMS was allowed to spread across the wafer, before the wafers were placed into an oven and stored at 100 °C for 24 hours. During this time, water adsorbed on the silica surface cleaves the PDMS backbone, and the resulting silanol-terminated PDMS subsequently undergoes a condensation reaction with the silica surface.[58] PDMS layers were washed with copious amounts of toluene, ethanol, and water, before being soaked in toluene for at least an hour to ensure complete removal of untethered polymer. Using this method, layer thickness could be tuned by increasing PDMS viscosity (i.e. chain length) or reaction time (i.e., grafting density). The reaction mechanism (as detailed by Graffius *et al.*[58]) is not trivial, and the length of grafted chains cannot be predicted simply by knowing the length of the precursor PDMS chains.[12] Here, physicochemical parameters are derived from previously published characterization.[12]

AFM measurements (Bruker Multimode 8 AFM with a Nanoscope 5 controller) were conducted with Bruker FMV-A tips, which were measured to have a spring constant of approximately 3 N/m. The Peakforce imaging mode was used to record a 256 by 256 array of force curves over a square area of side either 500 or 1000 nm (pixel length of 2 or 4 nm). The Peakforce setpoint was 5 nN, Peakforce frequency 2000 Hz, and scan rate 0.8 Hz. The Peakforce amplitude, which controls the length of the force curve, was adjusted between 30 and 60 nm for each sample, to minimise ringing and ensure an adequate baseline was captured before the tip encountered the surface. Generally, thicker layers required a higher Peakforce amplitude. All measurements were conducted on a clean sample in air.

Peakforce mapping produced 65,536 force curves, which were processed in a custom Python script which identified points 1-6 depicted in Fig. S7-S11 to produce maps of a range of parameters. Briefly, Peakforce files from the Multimode 8 were imported using the Bruker *Nanoscope* Python module. Jump-in points were found by interpolating the separation value where the approach curve reached 50% of the maximum adhesion force value. Maximum adhesion was taken as the 95% force percentile in the retraction curve. Further description, alongside the code required for the analysis, is supplied in Supplementary Information. The current version of this code is maintained on a Github repository.

Author contributions CN procured funding. CN and AG designed research. FR performed simulations. AT and AG supervised simulation work. IJG performed experiments.

CN supervised experiments. IJG, FR, AT, and AG analysed data. IJG and AG wrote the original draft of the paper; all authors edited the final version.

Acknowledgments

We thank Glen McHale and Erica Wanless for their insightful comments on the manuscript. The authors acknowledge funding from the Australian Research Council (FT180100214, DP230100555) and under the National Recovery and Resilience Plan (NRRP), Mission 4, Component 2, Investment 1.1, Call for tender No. 104 published on 2.2.2022 by the Italian Ministry of University and Research (MUR), funded by the European Union – NextGenerationEU– Project Title SoftNanoPores – CUP D53D23002240006 - Grant Assignment Decree No. 957 adopted on 30/06/2023 by the Italian Ministry of Ministry of University and Research (MUR). We acknowledge the EuroHPC Joint Undertaking for awarding access to the EuroHPC supercomputer LUMI, hosted by CSC (Finland) and the LUMI consortium through a EuroHPC Regular Access call.

Supporting Information

Supporting Information Available: length distribution of simulated chains compared to the Schulz-Zimm distribution obtained from experiments; details on simulations; average thickness of simulated PDMS layers; volume fractions of polydisperse and monodisperse layers; details of vertical phase separation; definition of reduced grafting density; effect of substrate deformation; calculation of surface area of the PDMS layers; modeling of CAH; details on AFM MFM mapping and code used to analyze data.

References

1. Gresham, I. J.; Neto, C. Advances and challenges in slippery covalently-attached liquid surfaces. *Adv. Colloid Interface Sci.* **2023**, *315*, 102906.

2. Chen, L.; Huang, S.; Ras, R. H.; Tian, X. Omniphobic liquid-like surfaces. *Nat. Rev. Chem.* **2023**, *7*, 123–137.

3. Peppou-Chapman, S.; Hong, J. K.; Waterhouse, A.; Neto, C. Life and death of liquid-infused surfaces: a review on the choice, analysis and fate of the infused liquid layer. *Chem. Soc. Rev.* **2020**, *49*, 3688–3715.

4. Scarratt, L.; Steiner, U.; Neto, C. A Review on the Mechanical and Thermodynamic Robustness of Superhydrophobic Surfaces. *Adv. Colloid Interface Sci.* **2017**, *246*, 133–152.

5. Giacomello, A.; Schimmele, L.; Dietrich, S.; Tasinkevych, M. Perpetual superhydrophobicity. *Soft Matter* **2016**, *12*, 8927–8934.

6. Chen, Y.; Yu, X.; Chen, L.; Liu, S.; Xu, X.; Zhao, S.; Huang, S.; Tian, X. Dynamic Poly(dimethylsiloxane) Brush Coating Shows Even Better Antiscaling Capability than the Low-Surface-Energy Fluorocarbon Counterpart. *Environ. Sci. Technol.* **2021**, *55*, 8839–8847.

7. Zhao, X.; Khandoker, M. A. R.; Golovin, K. Non-Fluorinated Omniphobic Paper with Ultralow Contact Angle Hysteresis. *ACS Appl. Mater. Interfaces* **2020**, *12*, 15748–15756.

8. Shabanian, S.; Zhao, X.; Au, S.; Furtak, N. T.; Golovin, K. Sustainable design of non-fluorinated yet oleophobic fibrous surfaces. *J. Mater. Chem. A* **2024**, *12*, 15716–15730.

9. Hauer, L.; Naga, A.; Badr, R. G. M.; Pham, J. T.; Wong, W. S. Y.; Vollmer, D. Wetting on silicone surfaces. *Soft Matter* **2024**, *20*, 5273–5295.

10. McHale, G.; Gao, N.; Wells, G. G.; Barrio-Zhang, H.; Ledesma-Aguilar, R. Friction Coefficients for Droplets on Solids: The Liquid–Solid Amontons' Laws. *Langmuir* **2022**, *38*, 4425–4433.

11. Lepikko, S.; Jaques, Y. M.; Junaid, M.; Backholm, M.; Lahtinen, J.; Julin, J.; Jokinen, V.; Sajavaara, T.; Sammalkorpi, M.; Foster, A. S.; Ras, R. H. A. Droplet slipperiness despite surface heterogeneity at molecular scale. *Nat. Chem.* **2024**, *16*, 506–513.

12. Gresham, I. J.; Lilley, S. G.; Nelson, A. R.; Koynov, K.; Neto, C. Nanostructure explains the behavior of slippery covalently attached liquid surfaces. *Angew. Chem.* **2023**, *62*, e202308008.

13. Wooh, S.; Vollmer, D. Silicone Brushes: Omniphobic Surfaces with Low Sliding Angles. *Angewandte Chemie International Edition* **2016**, *55*, 6822–6824.

14. Cheng, D. F.; Urata, C.; Masheder, B.; Hozumi, A. A Physical Approach To Specifically Improve the Mobility of Alkane Liquid Drops. *J. Am. Chem. Soc.* **2012**, *134*, 10191–10199.

15. Brittain, W. J.; Minko, S. A structural definition of polymer brushes. *J. Polym. Sci., Part A: Polym. Chem.* **2007**, *45*, 3505–3512.

16. Wang, L.; Mccarthy, T. J. Covalently Attached Liquids: Instant Omniphobic Surfaces with Unprecedented Repellency. *Angewandte Chemie International Edition* **2016**, *55*, 244–248.

17. Krumpfer, J. W.; McCarthy, T. J. Rediscovering Silicones: “Unreactive” Silicones React with Inorganic Surfaces. *Langmuir* **2011**, *27*, 11514–11519.

18. Flagg, D. H.; McCarthy, T. J. Rapid and Clean Covalent Attachment of Methylsiloxane Polymers and Oligomers to Silica Using B(C6F5)3 Catalysis. *Langmuir* **2017**, *33*, 8129–8139.

19. Zhou, X.; Wang, Y.; Li, X.; Sudersan, P.; Amann-Winkel, K.; Koynov, K.; Nagata, Y.; Berger, R.; Butt, H.-J. Thickness of Nanoscale Poly(Dimethylsiloxane) Layers Determines the Motion of Sliding Water Drops. *Adv. Mater.* **2024**, *36*, 2311470.

20. Sarma, J.; Zhang, L.; Guo, Z.; Dai, X. Sustainable icephobicity on durable quasi-liquid surface. *Chem. Eng. J.* **2022**, *431*.

21. Lhermerout, R.; Davitt, K. Contact angle dynamics on pseudo-brushes: Effects of polymer chain length and wetting liquid. *Colloids Surf. A* **2019**, *566*, 148–155.

22. Cambiaso, S.; Rasera, F.; Rossi, G.; Bochicchio, D. Development of a transferable coarse-grained model of polydimethylsiloxane. *Soft Matter* **2022**, *18*, 7887–7896.

23. Cambiaso, S.; Rasera, F.; Tinti, A.; Bochicchio, D.; Grosu, Y.; Rossi, G.; Giacomello, A. Local grafting heterogeneities control water intrusion and extrusion in nanopores. *Commun. Mater.* **2024**, *5*, 100.

24. Peppou-Chapman, S.; Neto, C. Mapping Depletion of Lubricant Films on Antibiofouling Wrinkled Slippery Surfaces. *ACS Appl. Mater. Interfaces* **2018**, *10*, 33669–33677.

25. Lhermerout, R.; Perrin, H.; Rolley, E.; Andreotti, B.; Davitt, K. A moving contact line as a rheometer for nanometric interfacial layers. *Nat. Commun.* **2016**, *7*, 12545.

26. Lee, T.; Hendy, S. C.; Neto, C. Interfacial flow of simple liquids on polymer brushes: Effect of solvent quality and grafting density. *Macromolecules* **2012**, *45*, 6241–6252.

27. Minko, S.; Müller, M.; Usov, D.; Scholl, A.; Froeck, C.; Stamm, M. Lateral versus perpendicular segregation in mixed polymer brushes. *Phys. Rev. Lett.* **2002**, *88*, 035502.

28. Müller, M. Phase diagram of a mixed polymer brush. *Phys. Rev. E* **2002**, *65*, 030802.

29. de Vos, W. M.; Leermakers, F. A. Modeling the structure of a polydisperse polymer brush. *Polymer* **2009**, *50*, 305–316.

30. Milner, S. T.; Witten, T. A.; Cates, M. E. Theory of the grafted polymer brush. *Macromolecules* **1988**, *21*, 2610–2619.

31. Milner, S. T.; Witten, T. A.; Cates, M. E. Effects of polydispersity in the end-grafted polymer brush. *Macromolecules* **1989**, *22*, 853–861.

32. Johnson, E. C.; Willott, J. D.; Gresham, I. J.; Murdoch, T. J.; Humphreys, B. A.; Prescott, S. W.; Nelson, A.; de Vos, W. M.; Webber, G. B.; Wanless, E. J. Enrichment of Charged Monomers Explains Non-monotonic Polymer Volume Fraction Profiles of Multi-stimulus Responsive Copolymer Brushes. *Langmuir* **2020**, *36*, 12460–12472.

33. Gresham, I. J.; Humphreys, B. A.; Willott, J. D.; Johnson, E. C.; Murdoch, T. J.; Webber, G. B.; Wanless, E. J.; Nelson, A. R. J.; Prescott, S. W. Geometrical Confinement Modulates the Thermoresponse of a Poly(N -isopropylacrylamide) Brush. *Macromolecules* **2021**, *54*, 2541–2550.

34. Abbott, S. B.; de Vos, W. M.; Mears, L. L. E.; Cattoz, B.; Skoda, M. W. A.; Barker, R.; Richardson, R. M.; Prescott, S. W. Is osmotic pressure relevant in the mechanical confinement of a polymer brush? *Macromolecules* **2015**, *48*, 2224–2234.

35. Lai, P. Y.; Zhulina, E. Structure of a bidisperse polymer brush: Monte Carlo simulation and self-consistent field results. *Macromolecules* **1992**, *25*, 5201–5207.

36. Lai, P.-Y.; Chen, J.-A. Stretch transition in a polymer brush. *Phys. Rev. E* **1995**, *51*, 2272.

37. Klushin, L.; Skvortsov, A. Critical dynamics of a polymer chain in a grafted monolayer. *Macromolecules* **1991**, *24*, 1549–1553.

38. Joanny, J. F.; de Gennes, P. G. A model for contact angle hysteresis. *J. Chem. Phys.* **1984**, *81*, 552–562.

39. Butt, H.-J.; Liu, J.; Koynov, K.; Straub, B.; Hinduja, C.; Roismann, I.; Berger, R.; Li, X.; Vollmer, D.; Steffen, W.; others Contact angle hysteresis. *Curr. Opin. Colloid Interface Sci.* **2022**, *59*, 101574.

40. Crassous, J.; Charlaix, E. Contact angle hysteresis on a heterogeneous surface: solution in the limit of a weakly distorted contact line. *Europhys Lett.* **1994**, *28*, 415.

41. Ramos, S. M. M.; Charlaix, E.; Benyagoub, A.; Toulemonde, M. Wetting on nanorough surfaces. *Phys. Rev. E* **2003**, *67*, 031604.

42. Giacomello, A.; Schimmele, L.; Dietrich, S. Wetting hysteresis induced by nanodefects. *Proc. Nat. Acad. Sci.* **2016**, *113*, E262–E271.

43. Extrand, C.; Kumagai, Y. Contact angles and hysteresis on soft surfaces. *J. Colloid Interface Sci.* **1996**, *184*, 191–200.

44. Limat, L. Straight contact lines on a soft, incompressible solid. *Eur. Phys. J. E* **2012**, *35*, 1–13.

45. Chen, L.; Bonaccurso, E.; Gambaryan-Roisman, T.; Starov, V.; Koursari, N.; Zhao, Y. Static and dynamic wetting of soft substrates. *Curr. Opin. Colloid Interface Sci.* **2018**, *36*, 46–57.

46. Fujii, Y.; Yang, Z.; Clough, A.; Tsui, O. K. Shear modulus of a polymer brush. *Macromolecules* **2010**, *43*, 4310–4313.

47. Fredrickson, G. H.; Ajdari, A.; Leibler, L.; Carton, J. P. Surface modes and deformation energy of a molten polymer brush. *Macromolecules* **1992**, *25*, 2882–2889.

48. Badr, R. G. M.; Hauer, L.; Vollmer, D.; Schmid, F. Cloaking Transition of Droplets on Lubricated Brushes. *J Phys Chem B* **2022**, *126*, 7047–7058.

49. Oliver, J.; Huh, C.; Mason, S. Resistance to spreading of liquids by sharp edges. *J. Colloid Interface Sci.* **1977**, *59*, 568–581.

50. Abraham, M. J.; Murtola, T.; Schulz, R.; Páll, S.; Smith, J. C.; Hess, B.; Lindahl, E. GROMACS: High performance molecular simulations through multi-level parallelism from laptops to supercomputers. *SoftwareX* **2015**, *1*, 19–25.

51. Souza, P. C.; Alessandri, R.; Barnoud, J.; Thallmair, S.; Faustino, I.; Grünewald, F.; Patmanidis, I.; Abdizadeh, H.; Bruininks, B. M.; Wassenaar, T. A.; others Martini 3: a general purpose force field for coarse-grained molecular dynamics. *Nat. Methods* **2021**, *18*, 382–388.

52. Kostakis, T.; Ettelaie, R.; Murray, B. S. Effect of high salt concentrations on the stabilization of bubbles by silica particles. *Langmuir* **2006**, *22*, 1273–1280.

53. Iannetti, L.; Cambiaso, S.; Rasera, F.; Giacomello, A.; Rossi, G.; Bochicchio, D.; Tinti, A. The surface tension of Martini 3 water mixtures. *J. Chem. Phys.* **2024**, *161*, 084707.

54. Schulz, G.; Dinglinger, A.; Husemann, E. Über die Kinetik der Kettenpolymerisationen. VII. *Z. Phys. Chem.* **1939**, *43*, 385–408.

55. Zimm, B. H. Apparatus and methods for measurement and interpretation of the angular variation of light scattering; preliminary results on polystyrene solutions. *J. Chem. Phys.* **1948**, *16*, 1099–1116.

56. Teisala, H.; Baumli, P.; Weber, S. A. L.; Vollmer, D.; Butt, H.-J. Grafting Silicone at Room Temperature—a Transparent, Scratch-resistant Nonstick Molecular Coating. *Langmuir* **2020**, *36*, 4416–4431.

57. Abbas, A.; Wells, G. G.; McHale, G.; Sefiane, K.; Orejon, D. Silicone Oil-Grafted Low-Hysteresis Water-Repellent Surfaces. *ACS Appl Mater Interfaces* **2023**, *15*, 11281–11295.

58. Graffius, G.; Bernardoni, F.; Fadeev, A. Y. Covalent Functionalization of Silica Surface Using "Inert" Poly(dimethylsiloxanes). *Langmuir* **2014**, *30*, 14797–14807.

Table of Contents Image

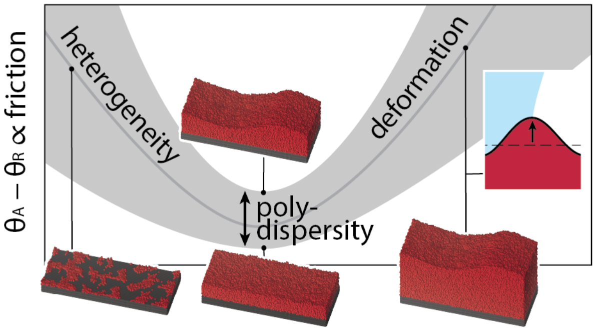

Thin polymer layers that exhibit vanishing droplet friction are achievable, but only with precise molecular control. The most pronounced slippery behavior occurs for smooth polydimethyl siloxane (PDMS) layers that are sufficiently thick to fully cover the substrate, are monodisperse and do not exhibit nanoscale waviness or layer deformation.